inorganics

MDPI

Article

$Gd_3Li_3Te_2O_{12}:U^{6+},Eu^{3+}$: A Tunable Red Emitting Garnet Showing Efficient U^{6+} to Eu^{3+} Energy Transfer at Room Temperature

David Böhnisch *, Juri Rosenboom, Thomas Jansen and Thomas Jüstel *

Department of Chemical Engineering, Münster University of Applied Sciences, Stegerwaldstrasse 39, D-48565 Steinfurt, Germany; juri.rosenboom@fh-muenster.de (J.R.); t.jansen@fh-muenster.de (T.J.)

* Correspondence: boehnisch.david@fh-muenster.de (D.B.); tj@fh-muenster.de (T.J.)

Received: 30 July 2018; Accepted: 21 August 2018; Published: 23 August 2018

Abstract: Since the invention of fluorescent light sources, there is strong interest in Eu^{3+} activated phosphors as they are able to provide a high color rendering index (CRI) and luminous efficacy, which will also hold for phosphor converted light emitting diodes. Due to an efficient U^{6+} to Eu^{3+} energy transfer in $Gd_3Li_3Te_2O_{12}:U^{6+},Eu^{3+}$, this inorganic composition shows red photoluminescence peaking at 611 nm. That means Eu^{3+} photoluminescence can be nicely sensitized via excitation into the U^{6+} excitation bands. Therefore, photoluminescence properties, such as temperature dependent emission and emission lifetime measurements, are presented. Charge transfer bands were investigated in detail. Additionally, density functional theory calculations reveal the band structure of the pure, i.e., non-doped host material. Obtained theoretical results were evaluated experimentally by the aid of diffuse UV reflectance spectroscopy.

Keywords: U^{6+} luminescence; Eu^{3+} luminescence; energy transfer; tunable emission spectra; temperature and time resolved spectroscopy

1. Introduction

In gas discharge light sources, Eu^{3+} activated phosphors (e.g., $Y_2O_3:Eu^{3+}$, $(Y,Gd)BO_3:Eu^{3+}$, and $Y(V,P)O_4:Eu^{3+}$) are widely applied to generate the red fraction of the white lamp spectrum [1,2]. Due to insufficient absorption in the blue spectral range, these phosphors are not applicable in combination with a blue emitting (In,Ga)N light emitting dioded (LED) [3–5]. Yet, line emitting Eu^{3+} activated phosphors possess promising properties such as high luminous efficacy, long-term stability, and they are capable of providing a high color-rendering index [6,7]. To improve the absorption cross-section, sensitizers like Bi^{3+} and Tb^{3+} are often used [6,8,9]. Additionally, Blasse and Krol reported about an energy transfer from U^{6+} to Eu^{3+} in several compounds. However, this energy transfer only occurs in most compounds at rather low temperatures [10,11]. To further investigate the energy transfer from U^{6+} to Eu^{3+}, we examined the luminescence properties of $Gd_3Li_3Te_2O_{12}:U^{6+},Eu^{3+}$. The luminescence properties of $Gd_3Li_3Te_2O_{12}:U^{6+}$, as well as $Gd_3Li_3Te_2O_{12}:Eu^{3+}$, were already described a few decades ago, but a co-doped sample has not been investigated so far [12,13]. The yttrium analogue is also well known when doped with U^{6+} and Eu^{3+}, respectively [14,15]. The excitation band of the uranate group in the Y^{3+} garnet is located at 325 nm and thus superimposes with the $^7F_0 \rightarrow {}^5H_J$ transitions of Eu^{3+} [14]. In case of the Gd^{3+} garnet, the excitation band is located at 340 nm, which allows one to solely excite the uranate group. This allows for a precise investigation of the energy transfer. Thereby, we strive for a deeper insight into the U^{6+} to Eu^{3+} energy transfer. Furthermore, we discuss the usefulness of U^{6+} as a sensitizer in the UV-A range for Eu^{3+} activated red-emitting phosphors.

The authors are aware that uranium is a radioactive and toxic element, so commercial use should not be a priority. Depleted uranium, which consists mainly of U^{238} isotopes, shows an alpha decay for the most part. With LED encapsulation, the alpha particles would not be emitted into the atmosphere, but are captured by the encapsulation. Consequently, the radiation exposure will be almost zero. Depleted uranium, however, is used as a ballast in space technology. No radiological and chemical toxicities were detected there [16]. Recent calculations demonstrated that the theoretically used amounts of uranium in LEDs would not even exceed the limits of German laws for 10 L of drinking water. Therefore, from our point of view, it is reasonable to investigate U^{6+} as a sensitizer for Eu^{3+} phosphors [17].

2. Method of Calculation and Electronic Properties

The Cambridge Serial Total Energy Package (CASTEP) Module of Materials Studio 8.0 (Devoloped by Accelrys) was applied to execute DFT calculations. A non-local sX-LDA functional (local density approximation, *abbrv.* LDA, with exchange contribution replaced by screeened exchange, *abbrv.* sX) was applied to the $Gd_3Li_3Te_2O_{12}$ host structure [18–20]. The entire calculation process used a plane-wave basis, linear response functions, norm-conserving pseudo potentials, Pulay density mixing schemes, and fine interpolation methods. If density mixing was not applicable, all bands/ensemble density functional theory (EDFT) was used. For a description of the interaction between the ionic cores and the valence electrons, the norm-conserving pseudopotentials were applied. The following electronic configurations were set in the calculations: Gd: [Xe] $4f^7 5d^1 6s^2$; Te: [Kr] $4d^{10} 5s^2 5p^4$; Li: [He]$2s^1$; O: [He] $2s^2 2p^4$. The Monkhorst-Pack k-points were set to $10 \times 10 \times 10$. The calculations were performed for a cubic cell. The energy convergence parameter was 5×10^{-6}.

The obtained band structure of $Gd_3Te_2Li_3O_{12}$ is depicted in Figure 1. The following direct band gap was derived from the calculations and determined to be ≈5 eV. This allowed us to classify this compound as a wide band-gap dielectric. Commonly, the usual LDA method underestimates the real band gap. The mean variation goes up to 40% [20,21]. More accurate band gap values are more likely to be expected with the sX-LDA approach. Therefore, we have selected the sX-LDA method for the calculations. An approach using UV reflectance spectroscopy described by Jüstel et al. to derive the optical band gap (Figure 2) served for a Kubelka-Muk transformed Tauc absorption spectrum. These experimental results were compared with the theoretical values [22–25].

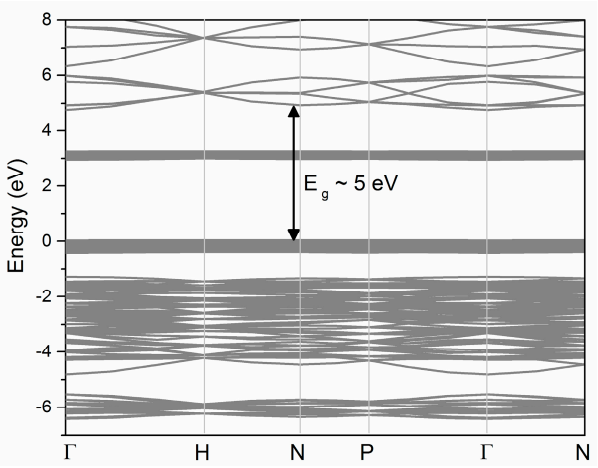

Figure 1. The calculated band structure of $Gd_3Li_3Te_2O_{12}$. sX-LDA calculated electronic bands are shown. The Fermi level is set to zero.

As demonstrated by the absorption spectrum (inset of Figure 2), the optical band gap amounts to ≈5 eV, which is in good accordance with the calculated value obtained from the sX-LDA method. The sX-LDA calculated density of states (DOS) diagrams are depicted in Figure 3. The conduction

band mainly consisted of the Te 5s and 5p, as well as the Li 2s states. The valence band (VB) had a width of ≈7 eV and exhibited several narrow sub-bands. The VB was dominated by O 2p states. In addition, the Gd 4f states showed a noteworthy contribution to the VB. In between, the Te 4p states had a major influence on the VB at around ≈6 eV. The wide band gap of the host, taken together with the experimental excitation spectra of U^{6+} in $Gd_3Te_2Li_3O_{12}$, allowed for the conclusion that the energy levels of the U^{6+} ion were located in the band gap.

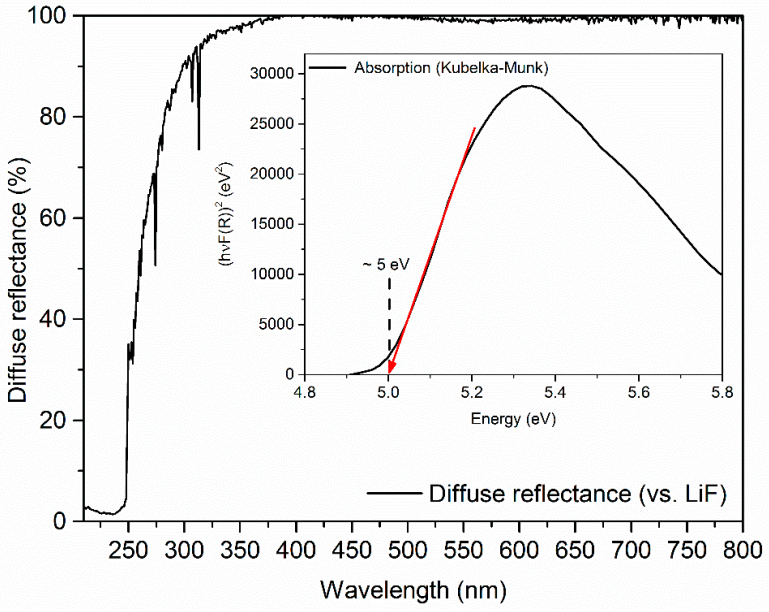

Figure 2. Tauc plot of $Gd_3Li_3Te_2O_{12}$ derived from a diffuse reflectance measurement.

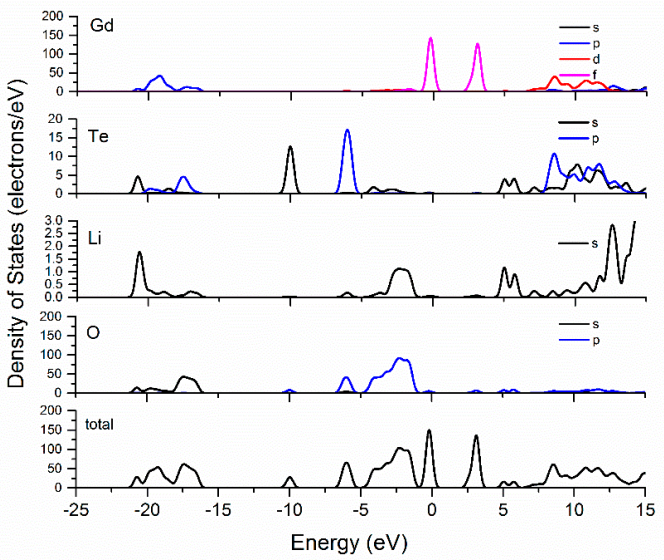

Figure 3. The calculated density of states diagrams for $Gd_3Li_3Te_2O_{12}$. From the top partial density of states is shown for Gd, Te, Li, and O ions, respectively, together with the total density of states.

3. Results and Discussion

The recorded XRD patterns as depicted in Figure 4 indicate the formation of cubic $Gd_3Li_3Te_2O_{12}$ and $Eu_3Li_3Te_2O_{12}$ in the space group $Ia\bar{3}d$ [15,26]. As in a typical garnet structure, Li atoms occupied the tetrahedral sites, and Te and Gd atoms were coordinated in octahedral and square antiprism geometry,

respectively. Due to the coinciding ionic radii of Gd^{3+} (105 pm) and Eu^{3+} (106 pm) in eightfold coordination, no changes in the structure could be observed upon substituting Gd^{3+} with Eu^{3+} [27]. The refined cell parameters of $Gd_3Li_3Te_2O_{12}$ with 1% U^{6+} were a = 1.2386 nm and V = 1.9003 nm^3, and for $Eu_3Li_3Te_2O_{12}$ with 1% U^{6+}, a = 1.2423 nm and V = 1.9176 nm^3, which nicely fit with literature data published before [26]. The intermediate samples with different Eu^{3+} content showed a linear behavior of the cell parameters. The critical U^{6+} concentration amounted to 1 mol % for the $[TeO_6]^{6-}$ site [14].

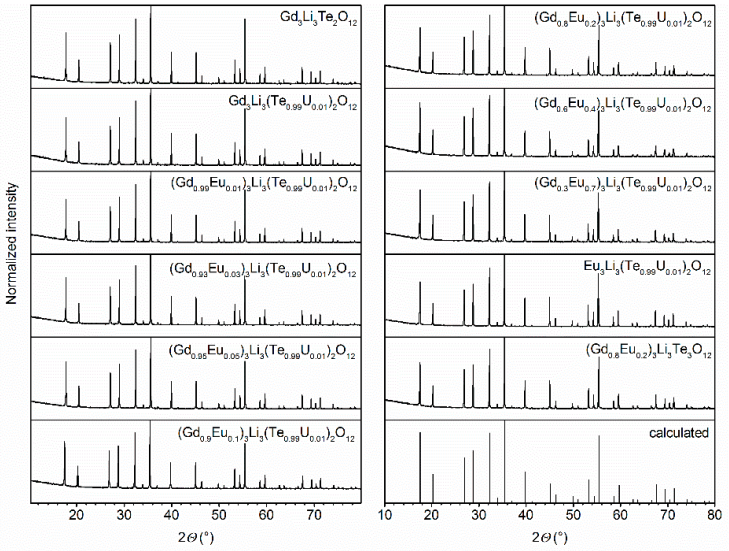

Figure 4. Powder XRD patterns of $Gd_3Li_3Te_2O_{12}$, $Gd_3Li_3(Te_{0.99}U_{0.01})_2O_{12}$, $(Gd_{0.8}Eu_{0.2})_3Li_3Te_2O_{12}$, and $(Gd_{1-x}Eu_x)_3Li_3(Te_{0.99}U_{0.01})_2O_{12}$ with $x = 0 \ldots 1$, as well as calculated reference pattern for Cu Kα radiation.

SEM micrographs of the sample $(Gd_{0.8}Eu_{0.2})_3Li_3(Te_{0.99}U_{0.01})_2O_{12}$, as shown in Figure 5, reveal a particle size of ≈1 µm, which form bigger agglomerates with a diameter of ≈20 µm. Samples doped with U^{6+} had a beige body color under natural light, indicating an absorption in the blue spectral range. Samples in the absence of U^{6+} exhibited a white body color.

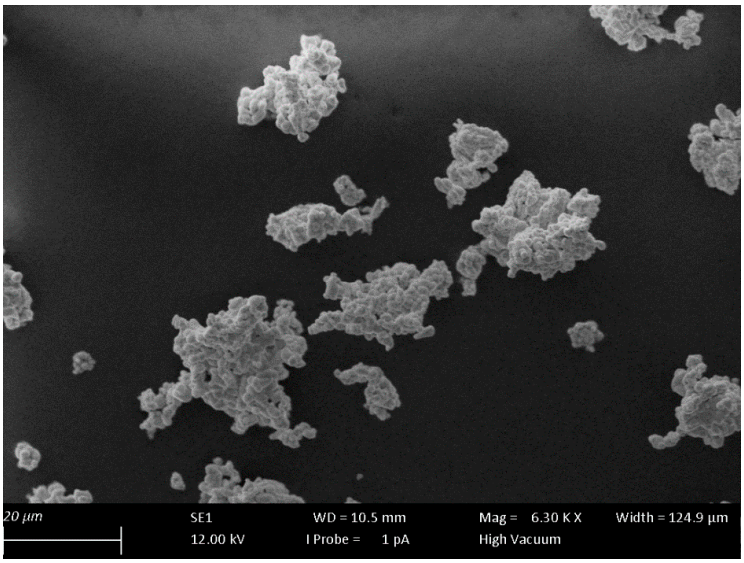

Figure 5. Scanning electron micrograph of $(Gd_{0.8}Eu_{0.2})_3Li_3(Te_{0.99}U_{0.01})_2O_{12}$ particles.

The body color could be derived from the reflectance spectra in Figure 6. $Gd_3Li_3Te_2O_{12}$ showed one strong absorption band at 250 nm. This could be assigned to the O^{2-} to Te^{6+} charge transfer (CT) in the $[TeO_6]^{6-}$ octahedron [13,28]. In addition, at 276 and 313 nm, Gd^{3+} transitions from the ground state $^8S_{7/2}$ to the ^6I_J and ^6P_J levels were observed. Incorporation of Eu^{3+} created an additional band at 260 nm representing the CT from O^{2-} to Eu^{3+}. The typical 4f → 4f transitions of Eu^{3+} were also correspondingly present. U^{6+} doped samples exhibited several absorption bands in the UV and blue–green spectral range. The precise assignment turned out to be difficult. Bands located in the UV range could tentatively be assigned to parity-allowed CT transitions involving the 6d level of U^{6+}, whereas parity-forbidden transitions involving the 5f level generated the absorption bands in the visible region [14,29].

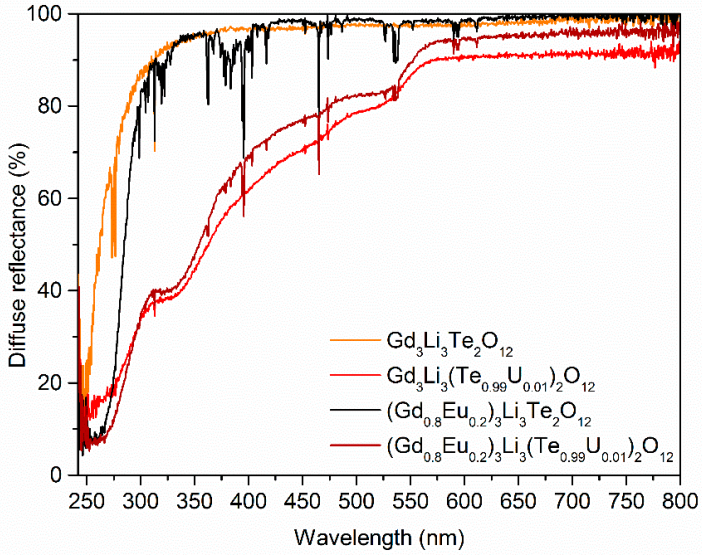

Figure 6. Diffuse reflectance spectra of $Gd_3Li_3Te_2O_{12}$ (orange line), $Gd_3Li_3(Te_{0.99}U_{0.01})_2O_{12}$ (red line), $(Gd_{0.8}Eu_{0.2})_3Li_3Te_2O_{12}$ (black line), and $(Gd_{0.8}Eu_{0.2})_3Li_3(Te_{0.99}U_{0.01})_2O_{12}$ (dark red line).

The excitation and emission spectra of the single and co-doped samples are plotted in Figure 7. $Gd_3Li_3(Te_{0.99}U_{0.01})_2O_{12}$ showed parity-forbidden U^{6+} emission in the octahedral coordination, peaking at 550 nm. At 3 K, a fine structure of the emission could be observed, revealing a zero-phonon line at 18,498 cm^{-1} with a high intensity due to the low site symmetry of the Te^{6+} site (S_6). Additionally, vibronic modes coupled with the CT transition could be identified. It was possible to assign some internal vibrational modes in the $[UO_6]^{6-}$ octahedron. Other than with the UO_2^{2+} emission, the coupling took place with more than one mode [14]. In addition, the ungerade vibrational modes dominated the coupling mechanism [30]. For ν_6 (T_{2u}), ν_4 (T_{1u}), and ν_3 (T_{1u}), we found energy values of 196, 299, and 576 cm^{-1}, respectively. The basic nature of the U^{6+} emission process is still not known. However, it was assumed that a charge-transfer transition between the O 2p and U 5f states led to the green emission [31]. In addition, coupling with ungerade vibrational modes indicated a parity-forbidden transition [32]. The emission spectra of the co-doped sample, as well as the Eu^{3+} doped sample, was dominated by the $^5D_0 \rightarrow {}^7F_2$ transition resulting from a low symmetry of the Gd^{3+} site (D_2). The excitation spectrum of the co-doped sample was evidence for the U^{6+} to Eu^{3+} energy transfer. While monitoring the $^5D_0 \rightarrow {}^7F_2$ transition of Eu^{3+}, the parity-allowed CTs of U^{6+} were observed. In addition, the Gd^{3+} to U^{6+} energy transfer, as described earlier by Smit and Blasse, was present [12]. Additionally, two excitation bands in the visible spectral range around 400 and 470 nm with rather low intensity could be observed, which match well with the diffuse reflectance spectra. In order to reveal the energetic positions of the CT bands, excitation spectra at 3 K were disentangled with the aid of Gaussian peak fitting. Figure 8a demonstrates that U^{6+} could be excited

via three different U^{6+} CT bands, peaking at 30,821, 29,303, and 35,435 cm^{-1}, as well as via the Te^{6+} CT band at 38,846 cm^{-1}. The Eu^{3+} emission could be excited through the Te^{6+} CT band and the Eu^{3+} CT band located at 37,202 cm^{-1}. The co-doped sample contained too many parameters, thus many possibilities were available to fit with Gaussian components. Hence, here the U^{6+} CT band was shifted from 35,435 towards 34,722 cm^{-1}.

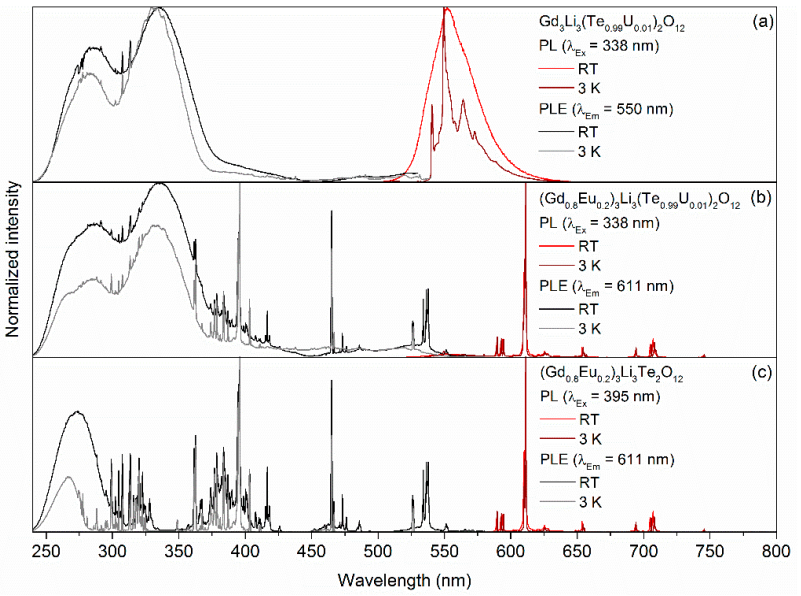

Figure 7. Emission and excitation spectra of (**a**) $Gd_3Li_3(Te_{0.99}U_{0.01})_2O_{12}$; (**b**) $(Gd_{0.8}Eu_{0.2})_3Li_3(Te_{0.99}U_{0.01})_2O_{12}$; and (**c**) $(Gd_{0.8}Eu_{0.2})_3Li_3Te_2O_{12}$ at room temperature and 3 K.

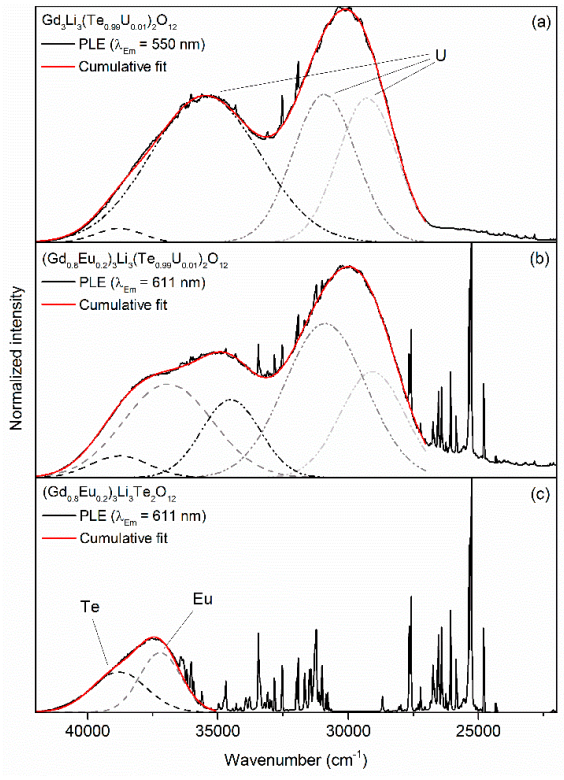

Figure 8. Excitation spectra with Gaussian distribution curves of (**a**) $Gd_3Li_3(Te_{0.99}U_{0.01})_2O_{12}$; (**b**) $(Gd_{0.8}Eu_{0.2})_3Li_3(Te_{0.99}U_{0.01})_2O_{12}$; and (**c**) $(Gd_{0.8}Eu_{0.2})_3Li_3Te_2O_{12}$ at 3 K.

Emission spectra of the solid solution according to $(Gd_{1-x}Eu_x)_3Li_3(Te_{0.99}U_{0.01})_2O_{12}$ with $0 \leq x \leq 1$ are depicted in Figure 9 and unveil that a Eu^{3+} concentration of 20% yielded the highest emission integral for the emission at 611 nm. With an increasing Eu^{3+} content, the emission integral of U^{6+} emission decreased, highlighting the energy transfer. In other words, after the excitation of the uranate group, the absorbed energy was transferred to Eu^{3+}. Therefore, the U^{6+} emission was hardly visible at a Eu^{3+} concentration higher than 10%. The samples were thus capable of generating green to red light under 338 nm excitation governed by the Eu^{3+} concentration. Color coordinates, as well as the luminous efficacies and the external quantum efficiencies, of each sample are listed in Table 1. We define the external quantum efficiency as the ratio of absorbed and emitted photons. The luminous efficacy decreased with increasing Eu^{3+} content as the emission was shifted from the green to the red spectral range, where the human eye is much less sensitive. The highest external quantum efficiency was reached at 10% Eu^{3+} and amounted to 42%. The quantum efficiency was thus rather low due to quenching of the U^{6+} CT process already at room temperature as well as some re-absorption in the red region as visible in the diffuse reflectance spectra [12]. In addition, due to the synthesis, the uranate group could show some mixed valence states, i.e., U^{5+}/U^{6+}. The resulting metal-to-metal charge transfer would decrease the external quantum efficiency as well as explain the slightly brownish body color. The quantum efficiency further decreased with increasing Eu^{3+} content. We thus suggest that the introduction of Eu^{3+} generated traps in the host compound and thus increased the overall defect concentration. Moreover, Eu^{3+} tends to show concentration quenching in some compounds, which further reduces the external quantum efficiency at higher Eu^{3+} concentrations [4,6,9,33]. At first, the traps were capable of inhibiting the quenching mechanism as we will discuss later. However, at higher Eu^{3+} concentrations, the number of defects was too advanced.

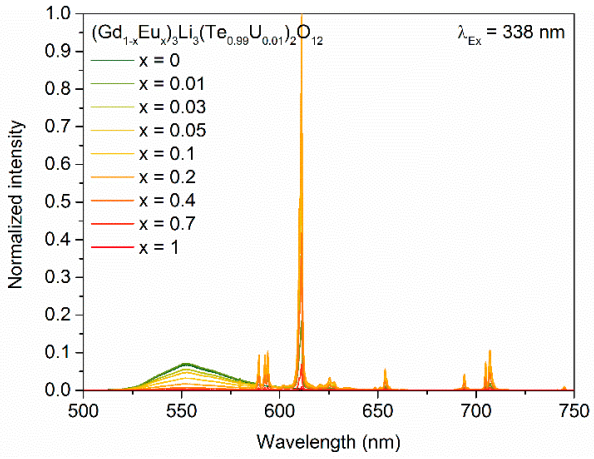

Figure 9. Emission spectra of $(Gd_{1-x}Eu_x)_3Li_3(Te_{0.99}U_{0.01})_2O_{12}$ with $0 \leq x \leq 1$ under 338 nm excitation.

Table 1. External quantum efficiencies, color coordinates, and luminous efficacy of $(Gd_{1-x}Eu_x)_3Li_3(Te_{0.99}U_{0.01})_2O_{12}$ with $0 \leq x \leq 1$ upon 338 nm excitation.

Eu^{3+} Conc. %	EQE (λ_{Ex} = 338 nm)	CIE1931 Color Coordinate		Luminous Efficacy [lm/W_{opt}]
		x	*y*	
0	32	0.3812	0.6119	632
1	39	0.4194	0.5748	576
3	39	0.4655	0.5297	511
5	41	0.5031	0.4931	464
10	42	0.5514	0.4459	405
20	38	0.5921	0.4061	357
40	16	0.5933	0.4048	352
70	2	0.5747	0.4224	364
100	<1	0.6079	0.3855	271

Fluorescence lifetime measurements monitoring the U^{6+} emission at 550 nm of co-doped $(Gd_{1-x}Eu_x)_3Li_3(Te_{0.99}U_{0.01})_2O_{12}$ with $0 \leq x \leq 0.2$ were conducted and plotted in Figure 10. The obtained decay curves with $x > 0$ could be well-fitted with a bi-exponential fitting function. The bi-exponential curve shape reflected the energy transfer from U^{6+} to Eu^{3+}. The single-doped sample exhibited only a mono-exponential behavior. Therefore, co-doping with Eu^{3+} led to a second mechanism in which manner the excited U^{6+} state could abate. The averaged fluorescence lifetimes τ of the U^{6+} emissions are listed in Table 2. With increasing Eu^{3+} content, the fluorescence lifetimes of the U^{6+} emission decrease. As energy transfer processes were often much faster than radiative transitions, this proved the presence of an energy transfer from U^{6+} to Eu^{3+} [34].

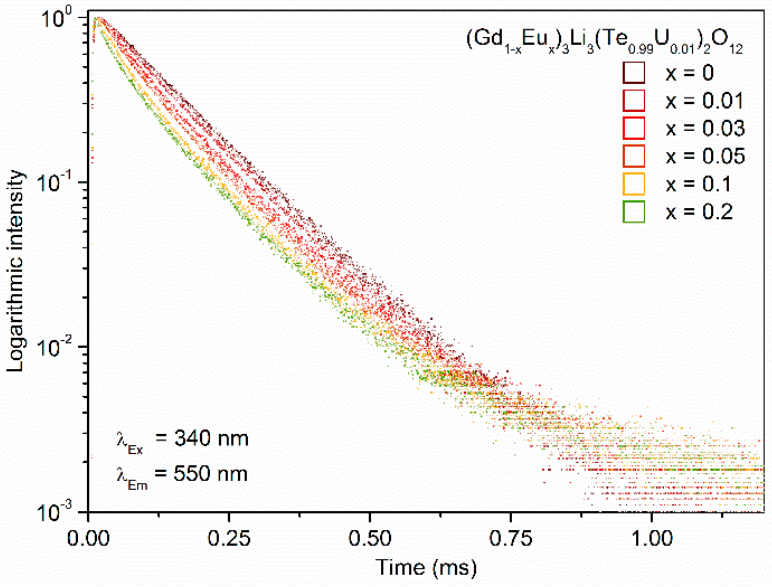

Figure 10. Fluorescence lifetime curves of $(Gd_{1-x}Eu_x)_3Li_3(Te_{0.99}U_{0.01})_2O_{12}$ with $0 \leq x \leq 0.2$ upon 340 nm excitation while monitoring the U^{6+} emission at 550 nm.

Table 2. Fluorescence lifetimes τ_1 and τ_2, as well as averaged lifetimes τ, of the U^{6+} emission in $(Gd_{1-x}Eu_x)_3Li_3(Te_{0.99}U_{0.01})_2O_{12}$.

Sample (x)	Fraction 1 (%)	τ_1 (µs)	Fraction 2 (%)	τ_2 (µs)	τ (µs)
0	100	127.5			
1	78	107.8	22	186.8	125.2
3	58	88.8	42	163.7	120.2
5	43	71.0	57	146.1	113.7
10	40	61.6	60	144.0	111.0
20	36	52.4	64	138.7	108.1

The decay time of U^{6+} at 3 K was found to be ≈250 µs and was shorter than in other compounds, e.g., ordered perovskites (300 µs), indicating a more allowed transition. Generally, the U^{6+} decay time strongly depended on the site symmetry, which became shorter when inversion symmetry was no longer present [31,32]. While U^{6+} was tentatively occupying the Te^{6+} site, it exhibited a local symmetry of S_6, which has no inversion center.

Emission spectra of U^{6+} at various temperatures are shown in Figure 11. At higher temperatures, the typical spectral broadening was observed. Already at 150 K, distinct phonon coupled transitions were visible. The determined emission integrals, as well as the emission lifetimes at different temperatures of single-doped $Gd_3Li_3(Te_{0.99}U_{0.01})_2O_{12}$, are depicted in Figure 12. The decrease of the decay time over increasing temperature was probably due to an increase of the transition

probability [33]. Due to orbital mixing, the parity-forbidden character was likely weakened, leading to shorter decay times. The deviation from the sigmoidal shape at higher temperatures was tentatively caused by another excited state, as presumed by Bleijenberg [35,36]. At higher temperatures, another excited level was populated, which exhibited a different decay time. The thermal quenching temperature $T_{1/2}$ of the emission intensity depends on the energy difference between the position of the excitation and emission band. With a difference of 11,825 cm^{-1}, the quenching temperature should be between 450 and 500 K, and thus lower than in $Y_3Li_3Te_2O_{12}$ ($T_{1/2}$ = 540 K) due to longer Te–O bond lengths in $Gd_3Li_3Te_2O_{12}$ [31]. The experimental results indicated a quenching temperature of around 475 K. Blasse also suggested that the process of temperature quenching occurs via three quenching states in the configurational-coordinate diagram since the low energy gap between the ground state and the emitting state would lead to a much lower quenching temperature [31]. Already at low temperatures, quenching sets in, which might be defect related since the external quantum efficiencies were rather low.

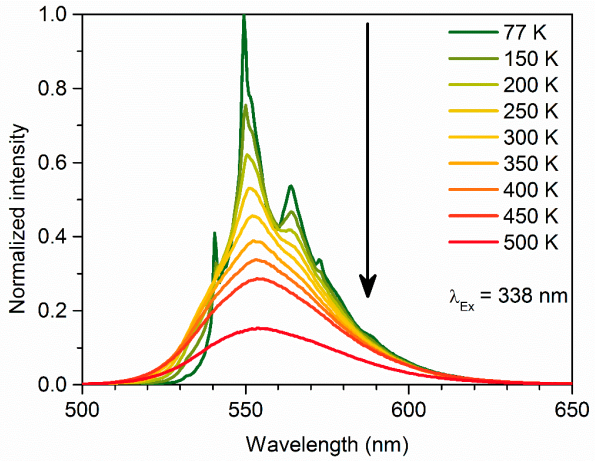

Figure 11. Emission spectra of $Gd_3Li_3(Te_{0.99}U_{0.01})_2O_{12}$ at various temperatures. Excitation wavelength was set to 338 nm.

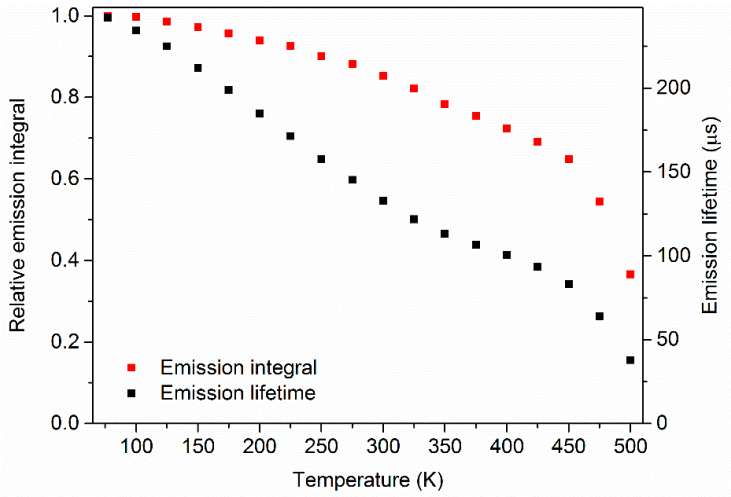

Figure 12. Emission integrals of U^{6+} excited at 338 nm, and averaged decay lifetimes monitoring the 550 nm emission of $Gd_3Li_3(Te_{0.99}U_{0.01})_2O_{12}$.

Figure 13 shows the temperature dependence of the emission intensity of Eu^{3+} excited by 338 nm radiation as well as emission lifetimes monitored at 611 nm of co-doped $(Gd_{0.8}Eu_{0.2})_3Li_3(Te_{0.99}U_{0.01})_2O_{12}$. The sample shows the typical quenching behavior with a thermal

quenching temperature of about 550 K. The quenching of the U^{6+} centered photoluminescence seemed to not affect the energy transfer from U^{6+} to Eu^{3+}. Thus, the energy transfer was a competitive process for the quenching mechanism. When the temperature-dependent U^{6+} emission of the same sample was investigated (Figure 14), it turned out that the quenching mechanism was somewhat hampered. The emission integrals started to decrease faster than the single-doped sample, but changed over to a plateau above 250 K. At higher temperatures, an increase could be observed. The decay measurements could only be fitted with a tri-exponential fit, emphasizing that several energy levels were present. The averaged decay lifetimes showed a similar behavior as the emission integrals. Due to orbital mixing, which weakened the parity regulation, the averaged emission lifetimes exhibited a more rapid decrease. At around 325 K, the lifetimes started to increase again, indicating that another energy level was populated. This phenomenon was more strongly pronounced than in the single-doped sample. The emission intensity, as well as the emission lifetimes, started to quench at around 475 K. Co-doping the sample with Eu^{3+} might have introduced some traps that prevented the reach of the cross-over point, which led to a relaxation into the ground-state level.

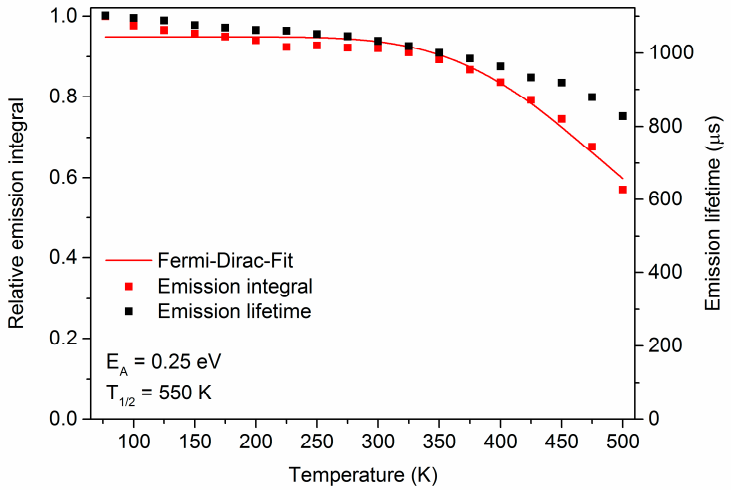

Figure 13. Emission integrals of Eu^{3+} excited at 338 nm, and averaged decay lifetimes monitoring the 611 nm emission of $(Gd_{0.8}Eu_{0.2})_3Li_3(Te_{0.99}U_{0.01})_2O_{12}$.

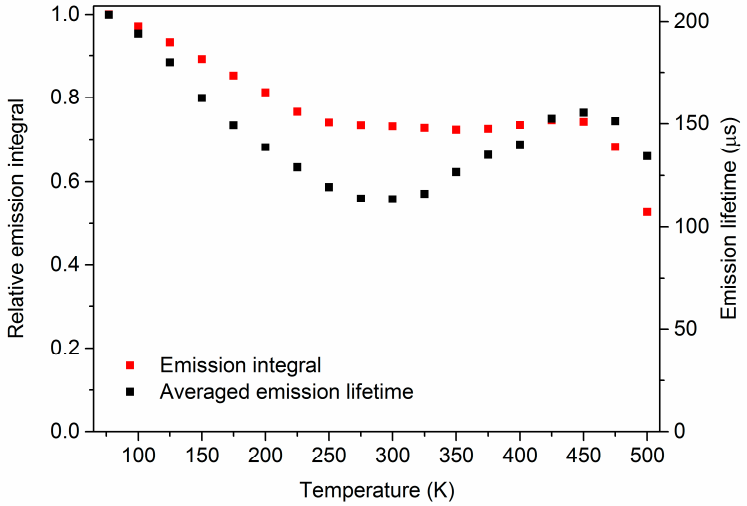

Figure 14. Emission integrals of U^{6+} excited at 338 nm, and averaged decay lifetimes monitoring the 550 nm emission of $(Gd_{0.8}Eu_{0.2})_3Li_3(Te_{0.99}U_{0.01})_2O_{12}$.

4. Experimental Section

A solid solution series of $(Gd_{1-x}Eu_x)_3Li_3Te_2O_{12}:U^{6+}$ was prepared using a conventional solid state reaction. The U^{6+} concentration was set to 1 at % relative to the Te site to avoid possible concentration quenching [14]. High purity reagents Gd_2O_3 (Treibacher, Althofen, Austria, 99.99%), Li_2CO_3 (Alfa Aesar, Ward Hill, MA, USA, 99%), TeO_2 (Alfa Aesar, 99.99%), Eu_2O_3 (Treibacher, 99.99%), and $UO_2(NO_3)_2 \cdot 6H_2O$ (made of uranium metal, Merck KGaA, Darmstadt, Germany, 99.99%) were weighed in stoichiometric amounts and rigorously mixed with hexane in an agate mortar. The dried blends were transferred to corundum crucibles and fired at 900 °C for 10 h under flowing oxygen. All samples containing U^{6+} exhibited a beige body color. The non-doped sample and the sample doped only with Eu^{3+} showed a white body color.

Phase purity of the synthesized samples was controlled using powder X-ray diffraction (XRD). All XRD patterns were recorded on a Panalytical (Almelo, The Netherlands) X'Pert PRO MPD diffractometer working in Bragg-Brentano geometry using Cu Kα radiation.

Photoluminescence (PL) and photoluminescence excitation (PLE) spectra were recorded on an Edinburgh Instruments (Livingston, UK) FLS980 spectrometer equipped with a Xe arc lamp (450 W) and a Peltier cooled (−20 °C) single-photon counting photomultiplier (Hamamatsu (Hamamatsu, Japan), R2658P). The emission spectra were corrected by applying a correction file obtained from a tungsten incandescent lamp certified by the National Physical Laboratory UK.

For time resolved spectroscopy, a micro-second pulsed Xe lamp (Heraeus (Hanau, Germany) µF920H) was used.

Temperature dependent PL spectra measurements from 77 to 500 K were performed using an Oxford Instruments (Abingdon, UK) cryostat MicrostatN2. Liquid nitrogen was used as a cooling agent. The temperature stabilization time was set to 30 s with a tolerance of ±3 K. Measurements below 77 K were performed using an Oxford Instruments Optistat AC-V 12 closed cycle He-cryostat.

Diffuse reflectance spectra (DRS) were recorded on an Edinburgh Instruments FS920 spectrometer equipped with a Xe arc lamp (450 W), a Peltier cooled (−20 °C) single-photon counting photomultiplier (Hamamatsu R928), and a Spectralon (Labsphere, North Sutton, NH, USA) integration sphere. $BaSO_4$ (99.998%, Sigma Aldrich, St. Louis, MO, USA) was used as a reflectance standard. External quantum efficiencies (eQE) were determined using the approach of Kawamura et al. [37].

Scanning electron microscopy (SEM) micrographs were recorded on a Zeiss (Oberkochen, Germany) EVO MA10 equipped with a secondary electron detector. SEM was operated in high vacuum mode (P = 10^{-7} Pa).

5. Conclusions

Solid solutions according to the formula $(Gd_{1-x}Eu_x)_3Li_3(Te_{0.99}U_{0.01})_2O_{12}$ with $x = 0 \ldots 1$ were successfully synthesized via a conventional solid-state reaction. Diffuse UV reflectance spectroscopy, as well as DFT calculations, revealed the band structure of the host. The band gap was determined to be about 5 eV, both from theory and from experiment. Photoluminescence measurements revealed that $Gd_3Li_3Te_2O_{12}:U^{6+},Eu^{3+}$ was capable of generating green band and red line emission peaking at 550 and 611 nm, respectively. At low temperatures, vibronic modes coupled to U^{6+} emission became visible, allowing the assignment of the energy of some ungerade vibrations. A distinct zero-phonon line was observed at 540.60 nm. Several excitation bands could be assigned to CT transitions from O^{2-} to Te^{6+}, U^{6+}, and Eu^{3+}, demonstrating the presence of efficient energy transfer from U^{6+} to Eu^{3+} even at high temperatures. Temperature-resolved photoluminescence and emission lifetime measurements confirmed the assumptions of Blasse and Bleijenberg concerning the energy level structure of U^{6+}. The thermal quenching temperature of the 4f–4f intraconfigurational transitions of Eu^{3+} was found to be at 550 K, which was independent of the U^{6+} quenching mechanism. Finally, it turned out that the introduction of Eu^{3+} into the host structure generated traps, which hampered the quenching of U^{6+}.

Author Contributions: Conceptualization, D.B. and T.J. (Thomas Jüstel); Data curation, D.B. and J.R.; Formal analysis, D.B. and T.J. (Thomas Jansen); Investigation, D.B., J.R., T.J. (Thomas Jansen) and T.J. (Thomas Jüstel); Methdology, D.B. and J.R.; Supervision, T.J. (Thomas Jüstel); Writing-original draft, D.B.; Writing-review & editing, J.R., T.J. (Thomas Jansen) and T.J. (Thomas Jüstel).

Funding: The authors are grateful to Merck KGaA, Darmstadt, Germany for generous financial support.

Conflicts of Interest: The authors declare no conflict of interest.

References

1. Welker, T. Recent developments on phosphors for fluorescent lamps and cathode-ray tubes. *J. Lumin.* **1991**, *48–49*, 49–56. [CrossRef]
2. Feldmann, C.; Jüstel, T.; Ronda, C.R.; Schmidt, P.J. Inorganic Luminescent Materials: 100 Years of Research and Application. *Adv. Funct. Mater.* **2003**, *13*, 511–516. [CrossRef]
3. Baur, F.; Jüstel, T. New Red-Emitting Phosphor $La_2Zr_3(MoO_4)_9$:Eu^{3+} and the Influence of Host Absorption on its Luminescence Efficiency. *Aust. J. Chem.* **2015**, *68*, 1727. [CrossRef]
4. Katelnikovas, A.; Plewa, J.; Sakirzanovas, S.; Dutczak, D.; Enseling, D.; Baur, F.; Winkler, H.; Kareiva, A.; Jüstel, T. Synthesis and optical properties of $Li_3Ba_2La_3(MoO_4)_8$:Eu^{3+} powders and ceramics for pcLEDs. *J. Mater. Chem.* **2012**, *22*, 22126. [CrossRef]
5. Park, S.H.; Lee, K.H.; Unithrattil, S.; Yoon, H.S.; Jang, H.G.; Im, W.B. Melilite-Structure $CaYAl_3O_7$:Eu^{3+} Phosphor: Structural and Optical Characteristics for Near-UV LED-Based White Light. *J. Phys. Chem. C* **2012**, *116*, 26850–26856. [CrossRef]
6. Baur, F.; Glocker, F.; Jüstel, T. Photoluminescence and energy transfer rates and efficiencies in Eu^{3+} activated $Tb_2Mo_3O_{12}$. *J. Mater. Chem. C* **2015**, *3*, 2054–2064. [CrossRef]
7. Žukauskas, A.; Vaicekauskas, R.; Ivanauskas, F.; Vaitkevičius, H.; Shur, M.S. Spectral optimization of phosphor-conversion light-emitting diodes for ultimate color rendering. *Appl. Phys. Lett.* **2008**, *93*, 51115. [CrossRef]
8. Park, W.J.; Jung, M.K.; Yoon, D.H. Influence of Eu^{3+}, Bi^{3+} co-doping content on photoluminescence of YVO_4 red phosphors induced by ultraviolet excitation. *Sens. Actuator B Chem.* **2007**, *126*, 324–327. [CrossRef]
9. Böhnisch, D.; Baur, F.; Jüstel, T. Photoluminescence and energy transfer behavior of narrow band red light emitting $Li_3Ba_2Tb_3(MoO_4)_8$:Eu^{3+}. *Dalton Trans.* **2018**, *47*, 1520–1529. [CrossRef] [PubMed]
10. Blasse, G.; Krol, D.M. Energy transfer phenomena in ordered perovskites of the type $Sr_2Na_{0.5}Ln^{3+}{}_{0.5}X^{6+}O_6$. *J. Lumin.* **1981**, *22*, 389–396. [CrossRef]
11. Krol, D.M.; Ros, J.P.M.; Roos, A. The influence of crystal structure and chemical composition on the energy transfer processes in uranates. *J. Chem. Phys.* **1980**, *73*, 1521–1526. [CrossRef]
12. Smit, W.M.A.; Blasse, G. Luminescence and energy migration in the garnet $Gd_3Li_3Te_2O_{12}$ doped with several rare earths and uranium. *J. Solid State Chem.* **1986**, *63*, 308–315. [CrossRef]
13. Köngeter, B.; Kemmler-Sack, S. Photolumineszenz und Energeitransfer in Seltenerd-aktivierten Granat $Gd_3Te_2Li_3O_{12}$. *Z. Naturforsch. A* **1984**, *39a*, 490–494. [CrossRef]
14. Alberda, R.H.; Blasse, G. Luminescence in a new garnet phase with hexavalent metal ions. *J. Lumin.* **1976**, *12–13*, 687–692. [CrossRef]
15. Zhang, W.; Seo, H.J. Luminescence and structure of a novel red-emitting phosphor Eu^{3+}-doped tellurate garnet $Li_3Y_3Te_2O_{12}$. *J. Alloys Compd.* **2013**, *553*, 183–187. [CrossRef]
16. Sztajnkrycer, M.D.; Otten, E.J. Chemical and Radiological Toxicity of Depleted Uranium. *Mil. Med.* **2004**, *169*, 212–216. [CrossRef] [PubMed]
17. Baur, F.; Jüstel, T. Warm-white LED with ultra high luminous efficacy due to sensitisation of Eu 3+ photoluminescence by the uranyl moiety in $K_4(UO_2)Eu_2(Ge_2O_7)_2$. *J. Mater. Chem. C* **2018**, *7*, 1600826. [CrossRef]
18. Clark, S.J.; Segall, M.D.; Pickard, C.J.; Hasnip, P.J.; Probert, M.I.J.; Refson, K.; Payne, M.C. First principles methods using CASTEP. *Z. Kristallogr.* **2005**, *220*, 567–570. [CrossRef]
19. Ceperley, D.M.; Alder, B.J. Ground State of the Electron Gas by a Stochastic Method. Phys. *Rev. Lett.* **1980**, *45*, 566–569. [CrossRef]
20. Perdew, J.P. Density functional theory and the band gap problem. *Int. J. Quantum Chem.* **1986**, *30*, 451. [CrossRef]

21. Perdew, J.P.; Zunger, A. Self-interaction correction to density-functional approximations for many-electron systems. *Phys. Rev. B* **1981**, *23*, 5048–5079. [CrossRef]
22. Enseling, D.; Herden, B.; Katelnikovas, A.; Möller, S.; Winkler, H.; Petry, R.; Meyer, H.-J.; Jüstel, T. Powder Reflection Spectroscopy in the Vacuum UV range. *J. Appl. Spectrosc.* **2014**, *81*, 341–346. [CrossRef]
23. Kubelka, P.; Munk, F. Ein Beitrag zur Optik der Farbanstriche. *Z. Phys.* **1931**, *12*, 593–601.
24. Tauc, J. Optical properties and electronic structure of amorphous Ge and Si. *Mater. Res. Bull.* **1968**, *3*, 37–46. [CrossRef]
25. Tauc, J.; Grigorovici, R.; Vancu, A. Optical Properties and Electronic Structure of Amorphous Germanium. *Phys. Stat. Sol.* **1966**, *15*, 627–637. [CrossRef]
26. O'Callaghan, M.P.; Lynham, D.R.; Cussen, E.J.; Chen, G.Z. Structure and Ionic-Transport Properties of Lithium-Containing Garnets $Li_3Ln_3Te_2O_{12}$ (Ln = Y, Pr, Nd, Sm–Lu). *Chem. Mater.* **2006**, *18*, 4681–4689. [CrossRef]
27. Shannon, R.D. Revised Effective Ionic Radii and Systematic Studies of Interatomic Distances in Halides and Chalcogenides. *Acta Crystallogr.* **1976**, *A32*, 751–767. [CrossRef]
28. Blasse, G.; Bril, A. Luminescence of tungsten-activated tellurates. *J. Solid State Chem.* **1970**, *2*, 291–294. [CrossRef]
29. Jørgensen, C.K.; Lundström, T.; Patoharju, O.; Noer, B.; Reio, L. Complexes of the 4d- and 5d-Groups. IV. Electron Transfer Bands with Special Application to M. Delépine's Complexes and a Transition from Iridium(III) to Pyridine, with some Remarks about Intermediate Coupling in Halide Complexes and the Uranyl Ion. *Acta Chem. Scand.* **1957**, *11*, 166–178. [CrossRef]
30. De Hair, J.T.W.; Blasse, G. Luminescence of the octahedral uranate group. *J. Lumin.* **1976**, *14*, 307–323. [CrossRef]
31. Blasse, G. The Structure Sensitivity of the U^{6+} Ion Luminescence in Oxides. *J. Electrochem. Soc.* **1977**, *124*, 1280. [CrossRef]
32. Blasse, G.; Bleijenberg, K.C.; Krol, D.M. The luminescence of hexavalent uranium in solids. *J. Lumin.* **1979**, *18-19*, 57–62. [CrossRef]
33. Chang, Y.-C.; Liang, C.-H.; Yan, S.-A.; Chang, Y.-S. Synthesis and Photoluminescence Characteristics of High Color Purity and Brightness $Li_3Ba_2Gd_3(MoO_4)_8$:Eu^{3+} Red Phosphors. *J. Phys. Chem. C* **2010**, *114*, 3645–3652. [CrossRef]
34. Blasse, G.; Grabmaier, B.C. *Luminescent Materials*; Springer Verlag: Utrecht, The Netherlands, 1994; pp. 91–106.
35. Bleijenberg, K.C.; Breddels, P.A. On the vibrational structure in the luminescence spectra of uranium-activated sodium fluoride crystals. *J. Chem. Phys.* **1980**, *72*, 5390–5398. [CrossRef]
36. Bleijenberg, K.C. Luminescence properties of uranate centres in solids. In *Luminescence and Energy Transfer. Structure and Bonding*; Springer Verlag: Utrecht, The Netherlands, 1980; pp. 97–217.
37. Kawamura, Y.; Sasabe, H.; Adachi, C. Simple Accurate System for Measuring Absolute Photoluminescence Quantum Efficiency in Organic Solid-State Thin Films. *Jpn. J. Appl. Phys.* **2004**, *43*, 7729–7730. [CrossRef]